aerospace

MDPI

Article

# Experimental and Numerical Study on the Combined Jet Impingement and Film Cooling of an Aero-Engine Afterburner Section

**Ashutosh Kumar Singh [1], Sourabh Kumar [2] and Kuldeep Singh [3,*]**

[1] Department of Mechanical Engineering, National Institute of Technology Manipur, Imphal 795004, India; ashutoshsingh@nitmanipur.ac.in
[2] Department of Mechanical Engineering, Indian Institute of Technology Delhi, New Delhi 110016, India
[3] Gas Turbine and Transmissions Research Centre, University of Nottingham, Nottingham NG7 2TU, UK
* Correspondence: kuldeep.singh@nottingham.ac.uk

**Abstract:** The recent advancement of cooling methodologies for critical components such as turbine blades, combustor liners, and afterburner liners has led to the development of a combination of impingement and film cooling. The present study proposes an efficient cooling technique for a modern aero-engine afterburner liner based on the combination of jet impingement and film cooling. To achieve this, a numerical model is devised to model the film flow over a corrugated liner with several jets impinging over it. The numerical model is validated in a set of in-house experiments as well as against experimental data available in the literature. The experiment is performed for a limited temperature range (i.e., with a low-density ratio). However, the numerical simulations are carried out by varying the blowing ratio from 0.3 to 0.6. The density ratio during the simulations is kept at 3.5. The minimum distance between the impinging plate and the liner is kept at h/D = 1. A detailed analysis of the numerical results indicates a significant drop in the temperature distribution over the liner surface because of the employed cooling technique. The present study also reveals that, under similar operating conditions, the combined jet impingement and film cooling system has the ability to achieve the targeted cooling effect at a lower bleed air flow rate due to its higher effectiveness than that of the standard film cooling arrangement.

**Keywords:** aeroengine; hydrogen combustion; film cooling; jet impingement; afterburner

check for updates

**Citation:** Singh, A.K.; Kumar, S.; Singh, K. Experimental and Numerical Study on the Combined Jet Impingement and Film Cooling of an Aero-Engine Afterburner Section. *Aerospace* **2023**, *10*, 589. https://doi.org/10.3390/aerospace10070589

Academic Editor: Jian Liu

Received: 23 May 2023
Revised: 23 June 2023
Accepted: 24 June 2023
Published: 27 June 2023



## 1. Introduction

Modern aeroengines are facing the difficult challenge of lessening their impact on the environment and increasing thrust at the same time. Aeroengines powered by hydrogen combustion are envisioned as cleaner aviation. However, it is difficult to create technology that is completely impenetrable. To overcome these obstacles and investigate hydrogen's potential as a workable fuel for aircraft engines, research and development initiatives are currently underway. To accomplish effective and low-emission hydrogen combustion in aeroengines, these efforts include looking at new combustion chamber designs, creating sophisticated fuel injection systems, examining alternate cooling techniques, and optimizing control tactics.

The afterburner section is used to increase the thrust of an aeroengine in specific circumstances, such as in combat or during takeoff from a short runway. The afterburner portion has additional fuel injectors and a supplemental air supply, and it is often situated below the primary combustion chamber. Figure 1 depicts the design of an aeroengine [1], including the cooling system and afterburner portion. In this part, extra fuel is burned in the turbine's exhaust stream. The temperature rises excessively and exceeds the threshold for the component's safe operation as a result of the combustion of the injected fuels. Hydrogen combustion tends to result in higher flame temperatures compared to those of hydrocarbon fuels, and therefore novel or hybrid cooling approaches are required to design an efficient cooling system. Therefore, afterburner components must be cooled in order to prevent thermally induced material failure. Improvements in gas turbine technology in recent years have led to more stringent requirements for the flow loss, combustion efficiency, and the aircraft's overall weight. Film cooling is often used to protect such critical parts from overheating and structural failures [2,3]. It prevents direct heating from hot flue gases by injecting a relatively lower temperature fluid which is commonly known as "coolant. The coolant fluid is typically injected through small surface holes or slots over the components that need protection. The injected coolant forms a thin layer over the surface and acts as a safeguard.

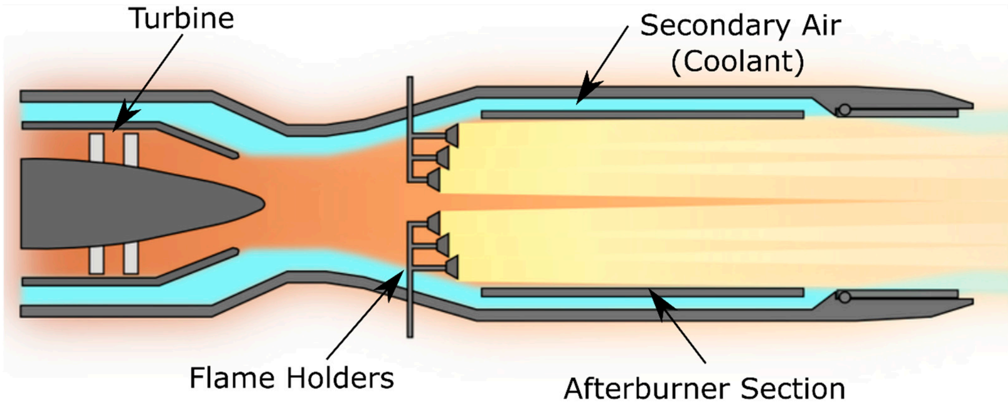


**Figure 1.** Aeroengine layout showing afterburner and cooling arrangement [1].

Since the coolant that facilitates the film cooling protection is generally extracted from the compressor, the whole process of film cooling results in a significant power loss. Moreover, the excessive use of coolant causes a lower thrust-to-weight ratio, which further reduces the combat, take-off and climb performance of the aircraft. Therefore, film cooling needs to be optimized for specific applications. Motivated by these challenges and applications, many authors have investigated this subject [4–9].

There are several parameters related to the film cooling phenomenon that have been investigated in the available literature. The main design variables of film cooling include the hole configuration, injection angle, orientation angle, and cooling surface configurations. The surface curvature is an essential parameter that governs the coolant coverage and jet lift-off. Numerous fundamental studies have been carried out to highlight the effect of surface curvature [10–13].

The wavy surface is one of the most common surface configurations used for combustor liners and aeroengines afterburners. The experimental study of Funazaki et al. [14] investigated the film cooling flow over a corrugated surface. Their experiments were conducted for a wide range of operating parameters, blowing ratios (2–4), Reynolds numbers (e.g., $1.6 \times 10^5$), and injection angles; they highlighted that the flow shows a similarity to the flat plate case, which is particularly close to the cooling holes. However, further downstream to the cooling hole, the flow decreases faster. Particularly, in the valley region, mixing with the heated mainstream is very high. The experimental investigations of Yong et al. [15] considered a sinusoidal corrugated test plate with desecrated cylindrical holes. In this study, the secondary air was injected into the mainstream through multiple rows of discrete cooling holes. They observed that there were distinct high- and low-temperature regions that, respectively, corresponded to the wave peaks and valleys of the corrugated liner. The corrugated liner improved the cooling effectiveness over the flat liner by 10% at a blowing ratio of 0.5 and 4.5% at a blowing ratio of 3.2. However, discharge coefficient varied only by 4.3% between the flat and corrugated surfaces.

The impact of the blowing ratio on the film cooling effectiveness and heat transfer coefficient of transverse corrugated surfaces was numerically investigated by Lihong et al. [16]. Their investigation considered the fixed density ratio (DR = 2.44), and the blowing ratio was adjusted to be between 1 and 2.5. They claimed that the wavy surface provided a relatively less uniform dispersion of coolant than a flat plate. Additionally, it had a significant effect on the heat transfer by the disruption of the boundary layer. Singh et al. [16] presented a thorough numerical analysis of the film cooling of a corrugated surface. Their study focused on an analysis of operating paraments, such as the effects of the blowing ratio, density ratio (DR), and injection angle. Their numerical simulations considered a wide range of DRs from 0.2 to 5.0 at a fixed mainstream Reynolds number of $1.5 \times 10^5$, three blowing ratios of 1, 2, and 3, and five injection angles from 30° to 90°. They reported that the corrugated surface profile significantly influenced the secondary stream flow. Additionally, the effectiveness of the film cooling of the corrugated surface increased linearly as the blowing ratio increased. The film cooling was significantly influenced by the injection angle and density ratio. The experimental and numerical study of Singh et al. [17] discussed a procedure to design a suitable injection configuration for corrugated liners. They reported the influence of different operating variables, including the mainstream Reynolds number, blowing ratio, and density. The blowing ratio varied from 0.8 to 3, and the mainstream Reynolds number varied from $10 \times 10^3$ to $4.5 \times 10^5$. The impact of the coolant injection angle was also reported by altering the injection from 45° to 90°. The study revealed that, contrary to the studies of film cooling on a flat plate, the blowing ratio increased at very high blowing ratios, and even with the afterburner's miniature cross section, the cooling hole injection angle was found to significantly affect film cooling. It was also found that as the injection angle increased from 45° to 90°, the effectiveness of the film cooling drastically decreased. The recent studies of Singh et al. [18] demonstrated the effect of various injection locations on the film cooling characteristics of a wavy surface. Their study claimed that the flow field and heat transfer were significantly influenced by the secondary stream positions. The same authors reported the effects of the performance of a double-slot injection location [19] on the film cooling characteristics of a sinusoidal corrugated surface.

The combination of impingement and film cooling is an effective method for the thermal management of hot sections. This combined cooling methodology has been exhaustively discussed by many researchers; they have reported the effect of the cooling hole shape, injection angle, impingement height (h/Di) [20,21], blowing ratio [22], Reynolds number [23], cooling hole design and configurations [21], operating pressure [23], surface coating effects [10], and plate materials [23]. Miao and Wu [22] numerically investigated the effect of three geometric shapes on cooling performance. One of the shapes considered for their study was of a cylindrical nature while other two were diffused holes in the forward and lateral directions. The effectiveness of the adiabatic film cooling and the flow field were significantly affected by the hole shape. In the cylindrical round, simple round angle (CYSA) and forward-diffused simple angle (FDSA), the counter-rotating vortex pair (CRVP) appears, whereas these vortices are not observed in LDSA holes at higher blowing ratios. Oh et al. [24] conducted an experimental analysis of the effects of the blowing ratio, impingement height (i.e., h/Di), and hole orientations angles by taking into account the plate's conduction effects. They concluded that, compared to a regular cooling hole, inclined cooling holes were shown to have superior cooling effectiveness. Additionally, variations in h/Di were found to be more significant for inclined holes.

The present study focuses on the combination of impingement and film cooling on the corrugated afterburner section of an aeroengine to provide optimal cooling. To the best of our knowledge, this is the first time a combination of impingement and film cooling has been attempted for afterburner applications. Both the experimental and numerical analyses are carried out to design an effective cooling configuration of the afterburner section. The experimental studies are performed at a density ratio of 1.09, as it is impractical to achieve a high temperature identical to aeroengine operating conditions in which the mainstream Reynolds number is kept identical to that of actual operating conditions of the afterburner section. A validated numerical model is utilized to extend our study to the actual operating conditions of an aeroengine afterburner section.

## 2. Problem Description

The present study is focused on analyzing the combined effect of jet impingement and the film cooling of the corrugated liner. The schematic of the geometry used for the study is shown in Figure 2. It consists of three cell zones, one each for the corrugated liner, impingement plate, and the fluid flow region. There are two references that have been picked to specify the geometry of the cooling configuration. The first reference is the cooling hole diameter (D) used for this study, which is equal to 2 mm. The second reference is the wavelength ($\lambda$) of the corrugated liner, which is 50D and equal to 100 mm. The maximum length of the domain is taken as 9$\lambda$ while the height of the domain is taken as 3.88$\lambda$. The front view of the domain is shown in Figure 2a. This figure also includes an expanded view from the right side of the channel. The top wall of the domain is situated a distance of 3.5D above the top surface of the impingement plate. Both the impingement plate and the corrugated liner are 2 mm thick, which are the same dimensions as those of the cooling holes. Since the corrugated liner is designed on a particular wavelength, the distance between the liner and the impingement plate is continuously changing. So, a minimum distance of 2 mm is always maintained between the two plates.

The cooling holes on the liner and impingement holes are placed in such a way that they will always be at an offset. Figure 2b shows the positions of the cooling and impingement holes used for the present study. As both plates are placed one above the other, the impingement plate is opaque to aid the visualization of the liner below it. Since both holes have a different frequency, the offset over a single wavelength of the corrugated liner first decreases from 3.75D to D and then again increases back to 3.75D. The full length of both plates is shown in Figure 2c. In the expanded view of the figure, the two sides of both the plates are named, which are used later in the details of the grid independence study. The two visible sides are the impingement plate: secondary fluid side and the liner: impingement plate side. Due to the current orientation of the plates, the back side of the plate is not visible; these are the impingement plate: liner side and the liner: mainstream flow side. In addition to the geometric parameters described above, the geometric as well as operational parameters are additionally shown in Table 1.

**Table 1.** Values and range of various parameters.

| Parameter | Value |
|---|---|
| Liner thickness, $t_l$ (mm) | 2.0 |
| Impingement plate thickness, $t_{impg}$ (mm) | 2.0 |
| Film cooling hole diameter, $D_f$ (mm) | 2.0 |
| Jet hole diameter, $D_i$ (mm) | 2.0 |
| The ratio of jet-to-plate spacing and jet diameter ($h/D_i$) with respect to flat portion of liner | 1.0 |
| Reynolds number based on mainstream flow and cooling hole diameter, $Re$ | 16,000 |
| Mainstream velocity (m/s) | 100 |
| Mainstream Pressure (bar) | 4 |
| Secondary air to mainstream pressure ratio | 1.25 |
| Blowing ratio, $M$ | 0.3–0.6 |
| Mainstream temperature (K) | 1750 |
| Density ratio, $DR$ | 3.5 |
| Secondary air temperature (K) | 500 |

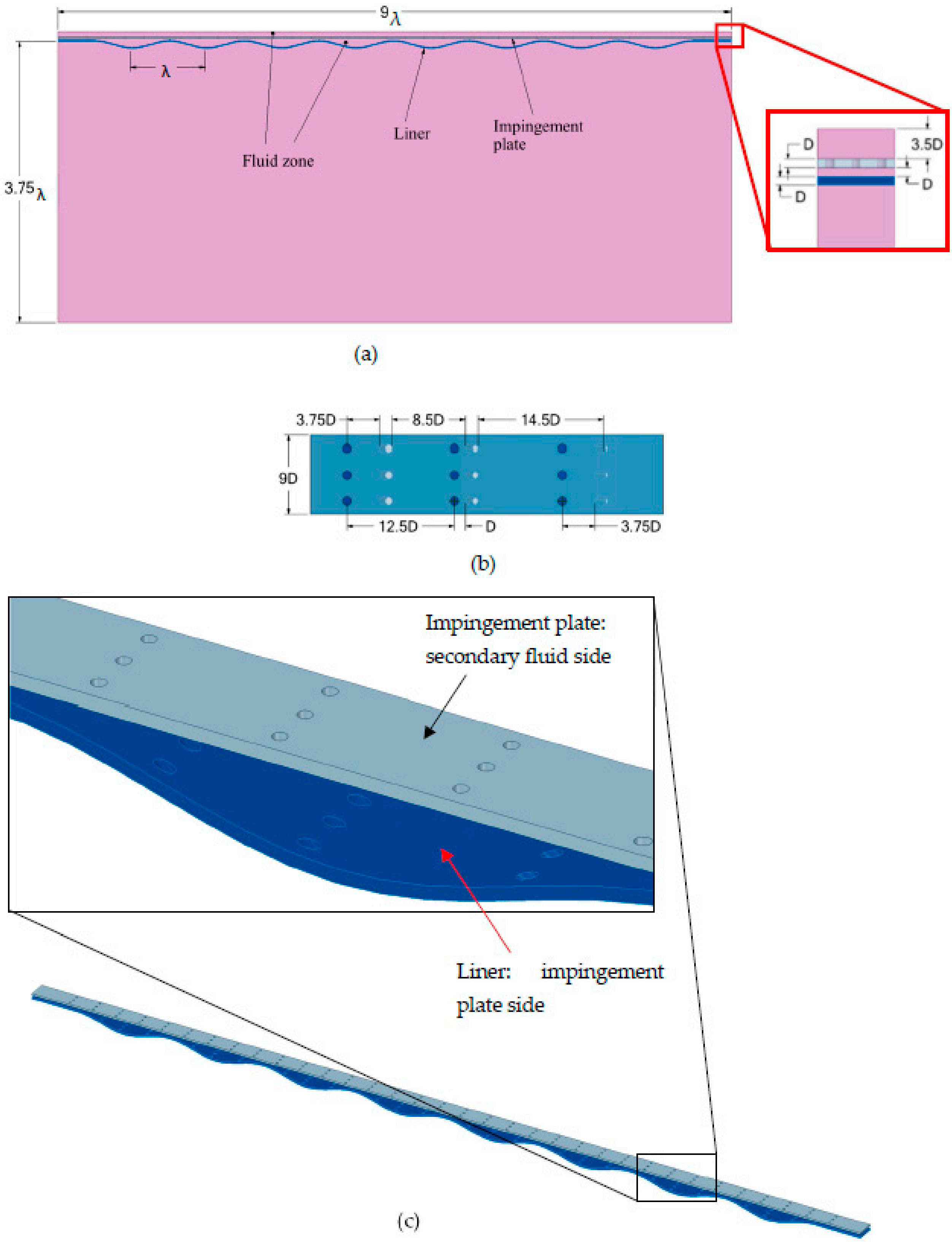


**Figure 2.** (**a**) Computational domain used for the study; (**b**) top view of the geometry along with the position of cooling holes on liner and impingement plate; and (**c**) detailed view of liner and impingement plate.

## 3. Experimental Setup and Measurement Procedure

In this work, experiments are conducted in a low-speed wind tunnel facility as depicted in Figure 3. As shown in Figure 3, the experimental setup includes two parts: mainstream path and secondary flow path. The mainstream is hot air whereas the coolant flow stream is cold air. The wind tunnel is suction type, and flow in the test section is regulated by the centrifugal blower. The wind tunnel flow velocity is derived by variable speed motor with a 5 HP capacity. The mainstream flow enters the test section via heating arrangements and a settling chamber. The test section is a square channel with a cross-sectional area of $200 \times 200$ mm$^2$ and is perfectly insulated with glass wool and Styrofoam to minimize the temperature drop along the test section. The test section is composed of low-thermal-conductivity material (acrylic = 0.2 W/m-K) and has the flexibility to install several types of mountings, such as an infrared camera, a test plate, and a plenum chamber for measurements. The secondary stream flow path includes a double-stage reciprocating compressor, pressure regulating valve, air filter and dehumidifier, and plenum chamber. The pressure regulator can be used in the 0–10 bar pressure range. The mass flow controller supplies the secondary air at flow rate of 0–3000 SLPM. The coolant stream is well mixed in the plenum before being injected onto the surface through the cooling holes. Both mainstream and coolant stream temperatures are measured with T-type thermocouples, whereas the cooling plate temperature is measured with infrared thermography (I.R. Camera, FLIR A325). The camera has a $320 \times 240$-pixel resolution and 60 Hz frame rate, and is able to capture thermal radiations in the spectral range of 7.5–13.0 µm. The mainstream flow velocity is measured with a pitot tube.

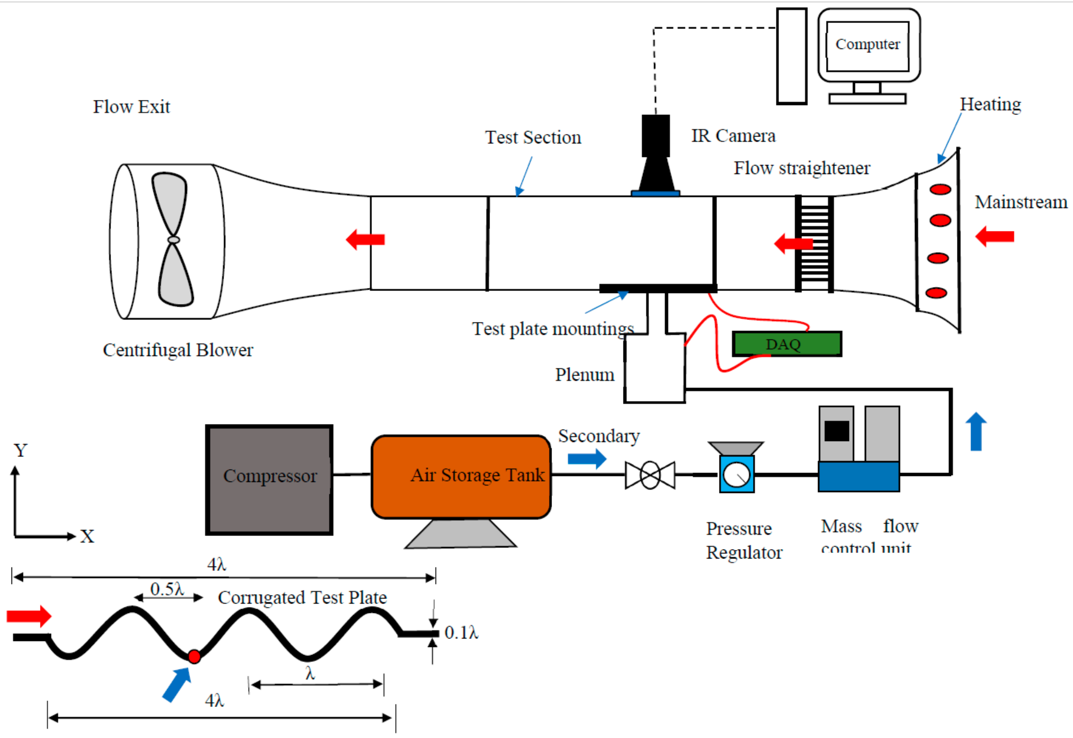


**Figure 3.** Schematics of experimental test facility used in the present study.

In the present experiment, the coolant secondary air is at comparatively lower temperature than that of the mainstream, which is heated air. T-type thermocouples mounted upstream of the test plate are used to measure the temperature of the mainstream. Similarly, the thermocouple in the plenum chamber is used to measure the temperature of the secondary stream. To achieve high surface emissivity (0.95), the film cooling surface is painted black with a matte finish. To obtain temperature distribution over the test plate, an infrared camera is mounted to capture the surface temperature. The supply of the primary and secondary streams is switched prior to data collection, and data recording is started once the system reaches a quasi-static condition. Once the mainstream reaches the quasi-static range, the camera is triggered to take images of film-cooled surface. The captured images of temperature profiles are further analyzed with help of research IR software. The measuring instruments are calibrated following the previous works of Singh et al. [25]. Table 2 provides a brief description of the equipment's measurement uncertainty in the present experimental study. The uncertainty is obtained based on the methodology described by Moffat [26]. The uncertainty in film cooling effectiveness is evaluated using the mathematical expression given in Equation (1). For the present study, the overall experimental uncertainty in film cooling effectiveness at 95% confidence level is reported to be in the range from 0.26 $\pm$ 0.0584 to 0.8 $\pm$ 0.0805.

$$\frac{\Delta\eta}{\eta} = \sqrt{\left(\frac{\partial\eta}{\partial T_{\text{sec}}}\Delta T_{\text{sec}}\right)^2 + \left(\frac{\partial\eta}{\partial T_{ms}}\Delta T_{ms}\right)^2 + \left(\frac{\partial\eta}{\partial T_s}\Delta T_s\right)^2} \tag{1}$$

**Table 2.** Details of instruments' measurement uncertainty in the present experimental study.

| S.N. | Instrument | Uncertainty |
|---|---|---|
| 1. | Infrared Camera | $\pm$1 K |
| 2. | Thermocouple | $\pm$0.5 K |
| 3. | Pitot Tube | $\pm$0.3% |
| 4. | Mass Flow Controller | $\pm$0.8% |

## 4. Numerical Methodology

As described in the problem description section, the computational domain consists of three zones, namely impinging plate, liner, and the fluid zone. The next step is to discretize the computational domain into several small cells to facilitate the solution of the governing equations. The description of the mesh used for this study is described later in the subsection Computational Domain. We will start our discussion with the governing equations used for the study.

### *4.1. Governing Equations*

The solution to the problem is obtained by solving three-dimensional governing equation for conservation of mass, momentum, and energy described below.

$$\frac{\partial\overline{u}_i}{\partial x_i} = 0 \tag{2}$$

$$\rho\overline{u}_j\frac{\partial\overline{u}_i}{\partial x_j} = -\frac{\partial\overline{p}}{\partial x_i} + \frac{\partial}{\partial x_j}\left[\mu\left(\frac{\partial\overline{u}_i}{\partial x_j} + \frac{\partial\overline{u}_j}{\partial x_i} - \rho u_i' u_j'\right)\right] \tag{3}$$

$$\rho\overline{u}_j\frac{\partial\overline{T}}{\partial x_j} = \frac{\partial}{\partial x_j}\left[\frac{\mu}{Pr}\left(\frac{\partial\overline{T}}{\partial x_j} - \rho T' u_j'\right)\right] \tag{4}$$

Since the simulations are carried out at higher Reynolds number, we need to model turbulence developed in the flow. So, to model the turbulence, the equations are modified using Reynolds averaging. Due to the averaging process, some new terms are added up in the governing equation while some of the terms are modified. In Equations (2)–(4), $\overline{u}_i$, $\overline{p}$, and $\overline{T}$ are the Reynolds averaged velocity, pressure, and temperature, while $u_i{}'$ and $T'$ are fluctuations in these respective quantities. The additional terms in the governing equations, such turbulent shear stress $-\rho u_i' u_j'$, are modeled as follows:

$$-u_i' u_j' = \nu_t\left(\frac{\partial\overline{u}_i}{\partial x_j} + \frac{\partial\overline{u}_j}{\partial x_i} - \frac{2}{3}k\delta_{ij}\right) \tag{5}$$

where $\nu_t$ is the additional turbulent viscosity added to dampen the effects of turbulence in the flow. In this work, the turbulent viscosity and other turbulence parameters such as turbulent kinetic energy TKE ($k$) and turbulent energy dissipation ($\varepsilon$) are modeled using realizable $k - \varepsilon$ model [26].

$$\rho \overline{u}_j \frac{\partial k}{\partial x_j} = \frac{\partial}{\partial x_j}\left[\left(\mu + \frac{\mu_t}{\sigma_k}\right)\frac{\partial k}{\partial x_j}\right] + G_k + G_b - \rho\varepsilon + S_k \tag{6}$$

$$\rho \overline{u}_j \frac{\partial \varepsilon}{\partial x_j} = \frac{\partial}{\partial x_j}\left[\left(\mu + \frac{\mu_t}{\sigma_\varepsilon}\right)\frac{\partial \varepsilon}{\partial x_j}\right] + \rho C_1 S\varepsilon - \rho C_2 \frac{\varepsilon^2}{k + \sqrt{\nu\varepsilon}} + C_{1\varepsilon}\frac{\varepsilon}{k} C_{3\varepsilon} G_b + S_\varepsilon \tag{7}$$

In Equations (6) and (7), $G_k$ is the generation of TKE due to mean velocity gradients, $G_b$ is the generation of the TKE due to buoyancy, $C_1$ is a function of the mean strain rate tensor $S$, $\sigma_k$ and $\sigma_\varepsilon$ are the turbulent Prandtl numbers, $C_2$ and $C_{1\varepsilon}$ are the constants, and $S_k$ and $S_\varepsilon$ are the source terms to the TKE and dissipation equations, respectively. Further, the turbulent viscosity discussed earlier is calculated as follows:

$$\nu_t = C_\mu \frac{k^2}{\varepsilon} \tag{8}$$

where $C_\mu$ is again the function of TKE, turbulence dissipation rate, mean strain rate tensor, and mean rotation rate tensor.

### *4.2. Computational Domain*

To solve this problem, the computational domain is divided into several cells using unstructured meshing. The meshing is performed using Ansys Fluent meshing mode. The discretization of the domain is performed using polyhex-core cells. Since the problem considered for this study involved conjugate heat transfer, both the solid and the fluid regions are discretized. Figure 4 shows the mesh used for the study. The boundary layer in the fluid region is resolved using prism layers with an inflation rate of 1.2 as we move away from the wall. In total, 5 prism layers are created to cover the entire boundary layer.

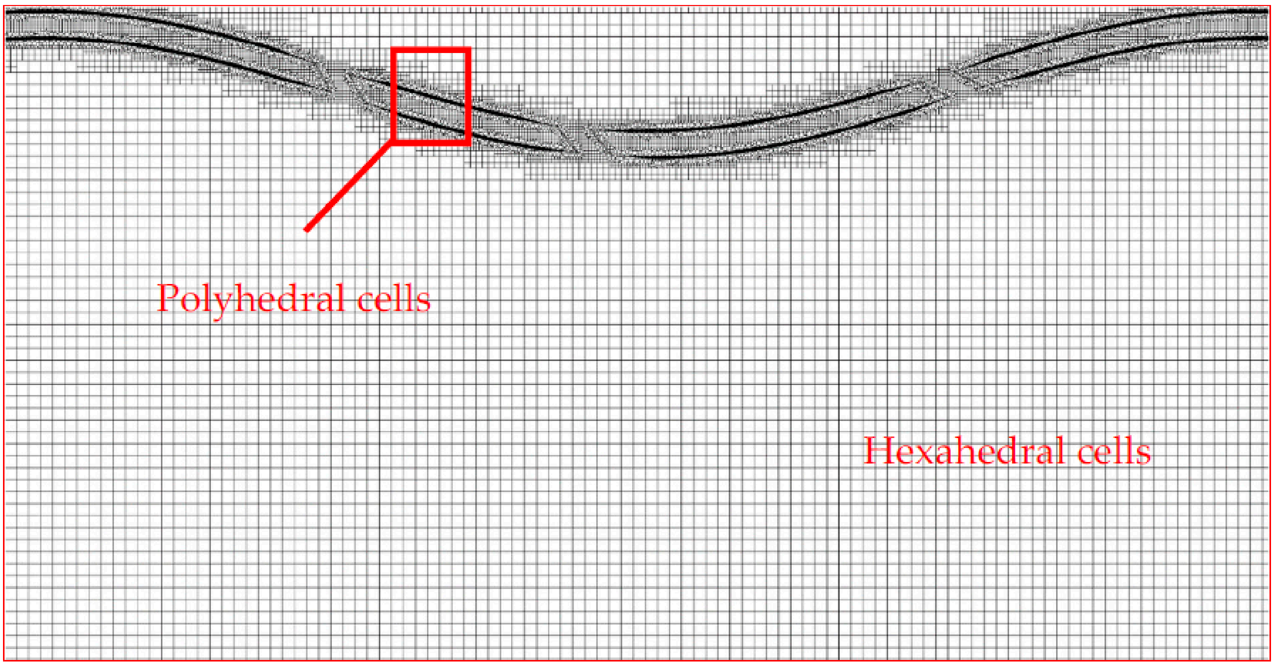


**Figure 4.** *Cont.*

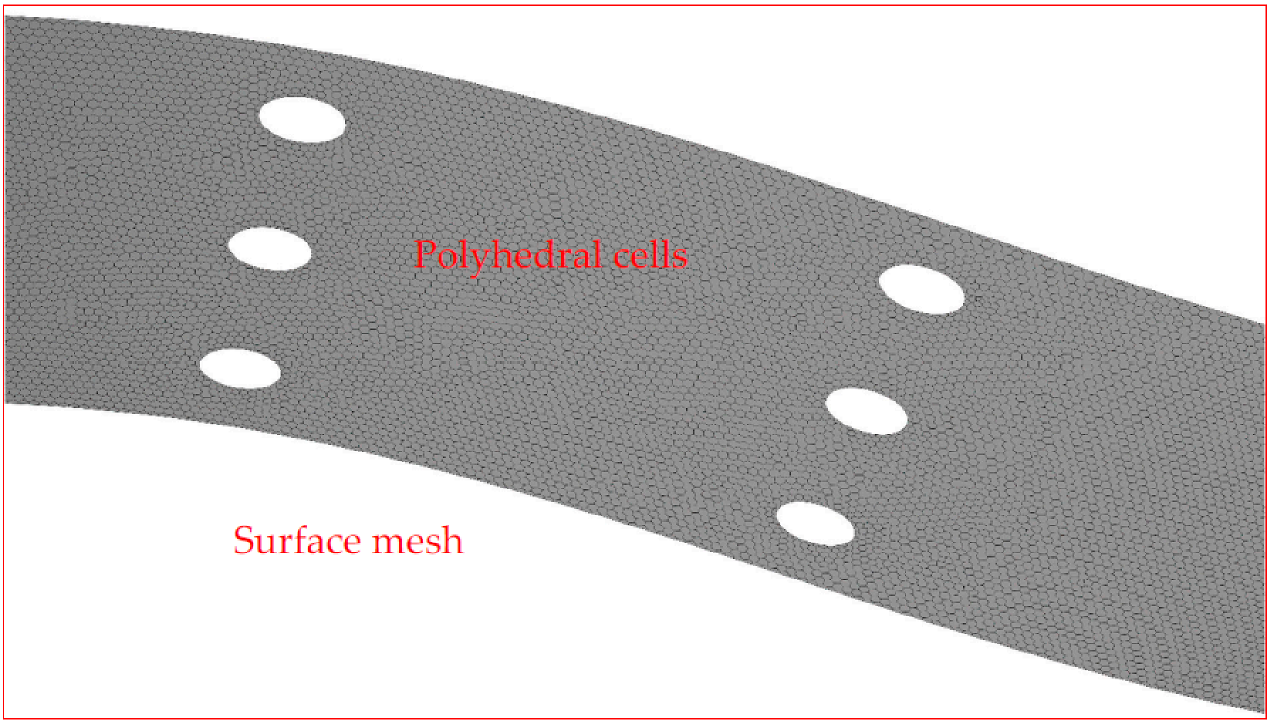


**Figure 4.** Discretization of the computational domain using polyhedral cells at the symmetric plane.

*4.3. Material Properties*

The simulations are carried out using air as the working fluid for both mainstream and the secondary fluid flow. The density of the fluid is calculated using the ideal gas approximation. Since there is large variation in the temperature of the fluid, the fluid properties, such as specific heat ($c_p$), conductivity ($k$), and viscosity ($\mu$), are described as polynomials of temperature in Kelvin [27].

$$c_p = \left(9.0813 \times 10^{-11}\right)T^4 - \left(4.8066 \times 10^{-07}\right)T^3 + \left(8.0735 \times 10^{-04}\right)T^2 - 0.32136T + 1045 \tag{9}$$

$$k_f = \left(7.9957 \times 10^{-12}\right)T^3 - \left(2.4013 \times 10^{-08}\right)T^2 + \left(8.3047 \times 10^{-05}\right)T + \left(2.8822 \times 10^{-03}\right) \tag{10}$$

$$\mu = \left(1.7020 \times 10^{-14}\right)T^3 - \left(4.0405 \times 10^{-11}\right)T^2 + \left(6.8539 \times 10^{-08}\right)T + \left(1.0616 \times 10^{-06}\right) \tag{11}$$

The liner material is also given temperature-dependent conductivity, as it varies significantly over the temperature range considered for this study [27].

$$c_p = -\left(2.994 \times 10^{-10}\right)T^4 + \left(8.038 \times 10^{-07}\right)T^3 - \left(3.934 \times 10^{-04}\right)T^2 - 0.01281T + 471.2 \tag{12}$$

$$k_s = \left(1.345 \times 10^{-11}\right)T^4 - \left(4.844 \times 10^{-08}\right)T^3 - \left(6.578 \times 10^{-05}\right)T^2 - (0.02637)T + 13.63 \tag{13}$$

*4.4. Boundary Conditions*

The domain considered for the present study consists of two inlets, one for the mainstream and another for the secondary flow. The velocity of fluid flow at the mainstream inlet is specified using the Reynolds number of the flow, while for the secondary flow, the velocity is determined using the values of the blowing ratio. Inlet temperature for the mainstream is fixed at 1750 K, while for the secondary flow, the inflow temperature is calculated from the density ratio. The turbulent intensity of both mainstream as well as secondary flow are fixed at 5% considering the operational conditions of the engines. There is only single outlet which is maintained at ambient pressure by specifying a zero-gauge pressure at the pressure outlet boundary during the simulations. The walls in the domain are given no-slip boundary condition. For the solution to energy equation in the solid cell zones, coupled boundary conditions are used to solve for the conjugate heat transfer.

*4.5. Solution Methodology*

The Reynolds averaged governing equations, Equations (2)–(4), and turbulent field variable equations, Equations (6) and (7), described earlier are discretized using finite volume method in Ansys Fluent solver. The equations are solved using a fixed value of initial condition and the boundary conditions specified in Section 4.4. The convective term of the governing equation is discretized using second-order upwind scheme. The pressure and velocity field of the solution are linked using SIMPLE algorithm [28]. The thermophysical properties of the materials used for the fluid and solid cell zones are also described during the solution setup. The equations are solved until the residuals for each equation except the energy equation fall below $10^{-5}$ level. For the energy equation, the residual is set at $10^{-8}$.

*4.6. Grid Independence Study*

Before commencing with the simulations for the problem, a grid independence study is carried out to minimize the errors induced by the grid size in the domain. Three difference grids with mesh size of 6.5 million (Mesh1), 11 million (Mesh2), and 22 million (Mesh3) are considered for the study. The resolution of boundary layer is an important aspect of the numerical simulations, especially when it involves heat transfer. The boundary layer in the fluid region is resolved using prism layers with an inflation rate of 1.2 as we move away from the wall. In total, 5 prism layers are created to cover the entire boundary layer, as shown in Figure 4. This study is carried out using a mainstream inlet velocity of 100 m/s and a blowing ratio of 0.6. The temperatures of the fluid at the mainstream inlet and secondary flow inlet are kept at 1750 K and 500 K, respectively.

Critical parameters in the current investigation are the non-dimensional temperature distribution on the impingement plate and corrugated liner. Consequently, significant care is used when perfecting grids in this area, and grid refinement factor (r) is taken to be 1.5 in this area. The different grids are compared for impingement plate on both side secondary flow and liner side for temperature distribution, as shown in Figure 5a,b. Non-dimensional temperature plot shows close agreement of M2 and M3 with maximum deviation of 0.75%. However, a maximum deviation of 5% is observed between M1 and M2 at $x/\lambda$ = 3.9. A similar trend is reported for impingement plate (liner side), as depicted in Figure 5b. The non-dimensional temperature plot shows close agreement of M2 and M3 with maximum deviation of 0.75%, and maximum deviation between M1 and M2 is 4.8%. Furthermore, the non-dimensional temperature plots for the corrugated line are shown in Figure 5c,d. Both curves exhibit similar trends on both impingement side and mainstream side. Figure 5c shows that both M2 and M3 are concurrent with maximum deviations of 0.5%. However, M1 and M2 show maximum deviation of 6% at $x/\lambda$ = 3.75. Similar to impingement side for liner, the mainstream side also shows concurrency of non-dimensional temperature plots for M2 and M3 with a maximum deviation of 0.6%, as shown in Figure 5d. Considering the balance between computation time and accuracy, the results presented here indicate that further refinement of the mesh will only lead to increase in the computational expenses without much improvement in the results. Hence, M2 is chosen for further investigation. The grid convergence index (GCI) method of uncertainty analysis by Celik and Li [29] is used to quantify discretization errors. The non-dimensional temperature ($\theta$) is chosen as the essential parameter for this study. The local order of accuracy ($p$) for the non-dimensional temperature lies in the range of $1.06 \leq p \leq 11.1$, with an overall average of 5.34. The numerical uncertainty caused by discretization errors is quantified in Figure 6. Figure 6a,b clearly represents the uncertainty for the critical parameters, such as effectiveness and non-dimensional temperature. The resulting numerical uncertainty is nearly constant for lateral effectiveness; however, a significant drop in uncertainty can be seen for average non-dimensional temperature. The uncertainty is higher along mainstream and monotonically decreases along the exhaust side, as shown in Figure 6b.

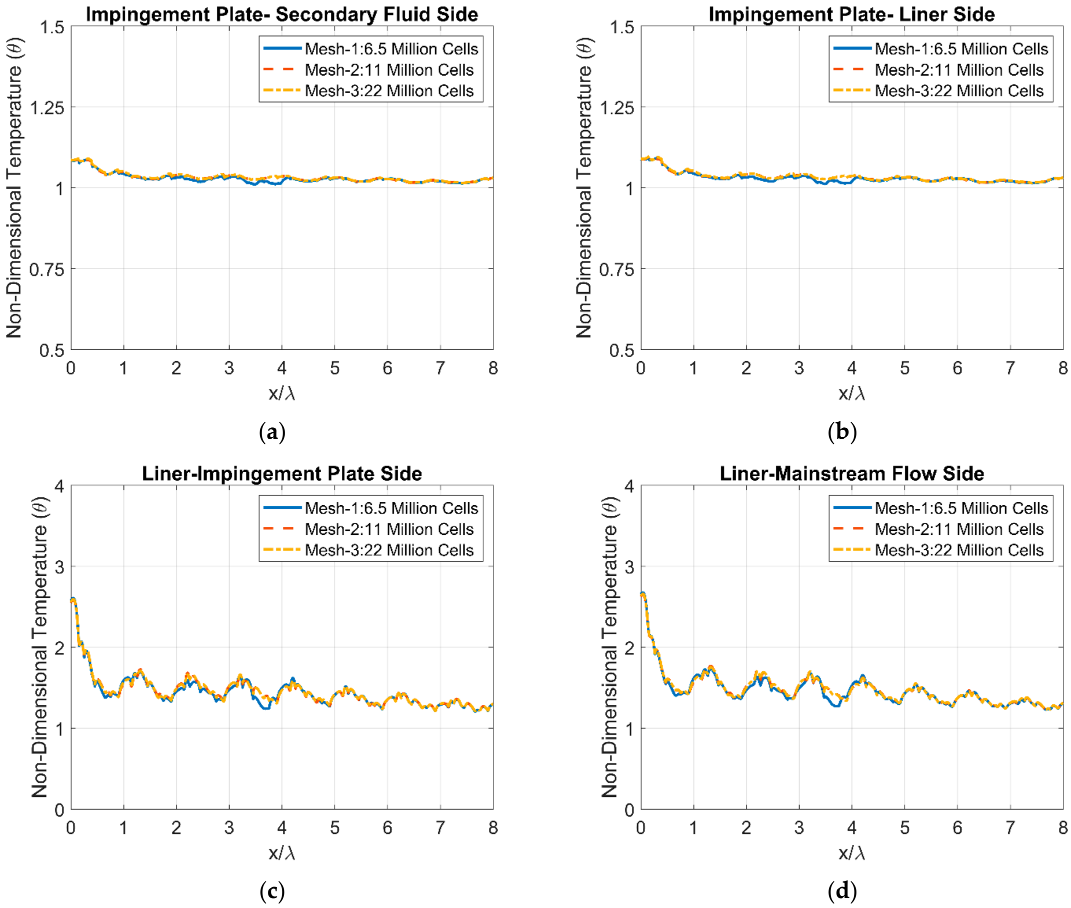


**Figure 5.** Grid independence study for the film cooling of a corrugated liner with jet impingement with a blowing ratio of 0.6 and density ratio of 3.5 (**a**) Impingement plate-secondary fluid side; (**b**) impingement plate-liner side; (**c**) Liner-impingement plate side; (**d**) Liner-mainstream flow side.

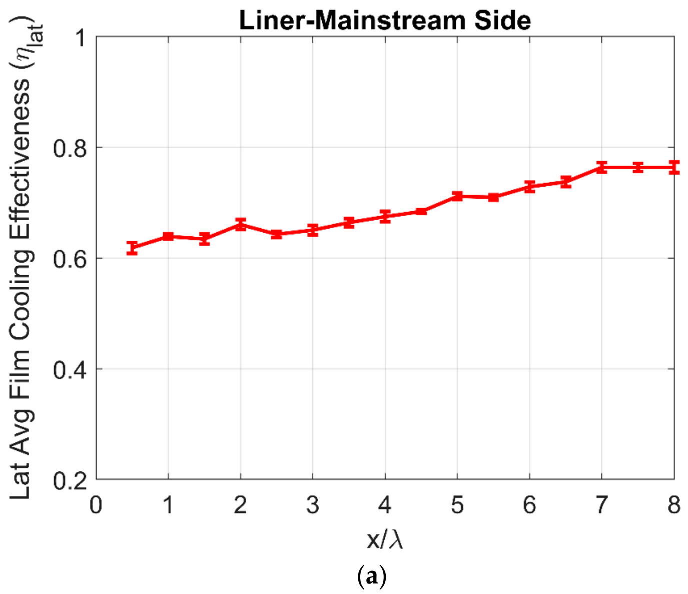


**Figure 6.** *Cont.*

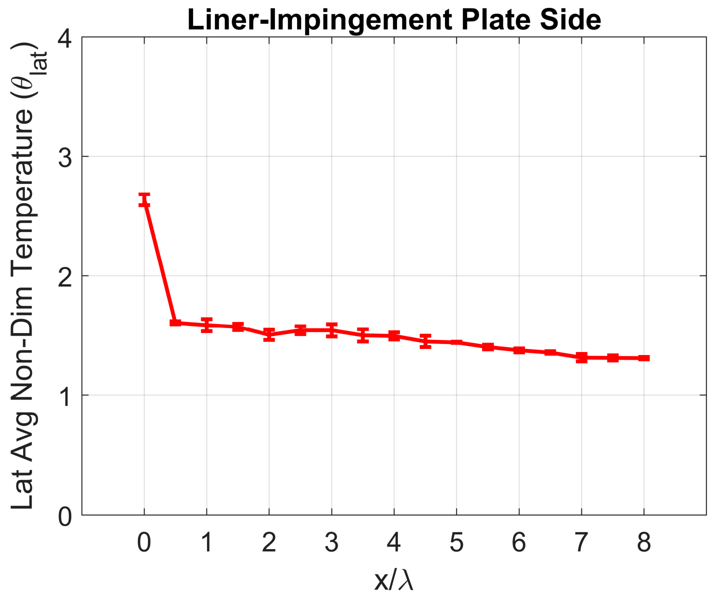


(**b**)

**Figure 6.** Numerical uncertainty for the film cooling of a corrugated liner with jet impingement with a blowing ratio of 0.6 and density ratio of 3.5. (**a**) Lateral average effectiveness; (**b**) lateral average non-dimensional wall temperature.

## 5. Results and Discussion

### *5.1. Validation of Numerical Methodology*

#### 5.1.1. Film Cooling on the Corrugated Surface

In the present study, an experimental study is carried out in order to compare the accuracy of the presented numerical model. The sinusoidal corrugated test plate is taken into consideration for the single injection location $L_{50}$, as shown in Figure 3. The corrugated plate employed in this study has a sinusoidal profile with wavelengths of (λ), lengths of (3λ), a lateral span of (2λ), and an amplitude-to-wavelength ratio of (a/λ = 0.05). The corrugated test plate is smooth, 3D printed, and made up of low-thermal-conductivity material, Nylon-12 (i.e., 0.16 W/mK). To protect the surface secondary stream of coolant, the stream is supplied through a plenum chamber with lengths of (3λ), a lateral span of (2λ), and a depth of (0.4λ). The plenum chamber is covered with glass wool and mounted in such a way that the secondary flow is well mixed before entering into the cross-flow domain. For the present experimental investigation, the mainstream flow is heated air at a flow velocity of 18 m/s, whereas the coolant stream of the secondary air is a relatively cold stream of air, such that a constant density ratio of DR = 1.095 can be maintained. The tests are carried out for the blowing ratio (M = 0.25) and density ratio (DR = 1.095) at a fixed injection angle of 45°, and the centerline effectiveness is plotted for comparison. The experimental measurement is plotted in the downstream direction of X/λ = 0 to 0.925, along with the uncertainty. The numerical model is two-dimensional, and for comparison purposes, all of the geometries, injection locations, and operating parameters are taken to be the same as those in the experimental case. The numerical simulations are carried out by considering the mainstream and secondary stream as the velocity inlets and the flow outlet as the pressure outlet. The all-solid domains are specified as having a no-slip adiabatic condition, except for the corrugated wall and coolant passages, for which a no-slip conjugated condition was assigned. A two-equation RANS (i.e., k-ε-Realizable) model is employed for the present validation, following the previous works of Singh et al. [17] on corrugated surfaces. They discussed the various turbulence models and their selection procedures for corrugated surface film cooling. The numerical trends of the variations in the experimental case are shown in Figure 7. The figure clearly shows that the numerical model shows a close prediction of the downstream location of X/λ = 0.2 to 0.25, and a overprediction is reported in the downstream of X/λ = 0 to 0.2. The same can be understood as a temperature drop in coolant passes due to the ionization of air, which further results in an increase in ineffectiveness. It closely captures the trends for effectiveness; therefore, it can be used for further study.

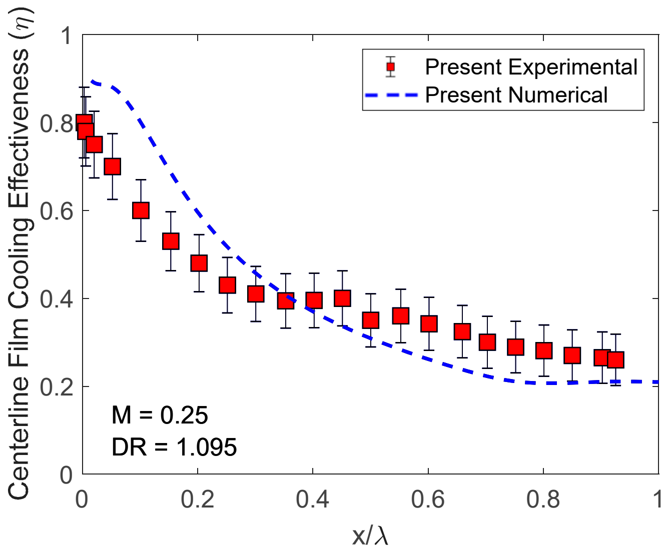


**Figure 7.** Validation of numerical model with the present experimental study of film cooling.

### 5.1.2. Combined Film Cooling and Jet Impingement Cooling

Since the combination of film cooling and jet impingement has not been studied previously, we carry out an additional validation of the combined cooling technique following the experimental study of Jung et al. [30] on a flat surface. The computational domain considered for this study is a representation of the test section considered in the experimental study. The centerline film cooling effectiveness measurements of Jung et al. [30] are plotted with the presented numerical model for M = 0.3 and h/Di = 1 in Figure 8. The figure clearly demonstrates that the numerical result for the centerline effectiveness follows the experimental trends, and the experimental uncertainty is within the range of x/D = 2.5 to 20.

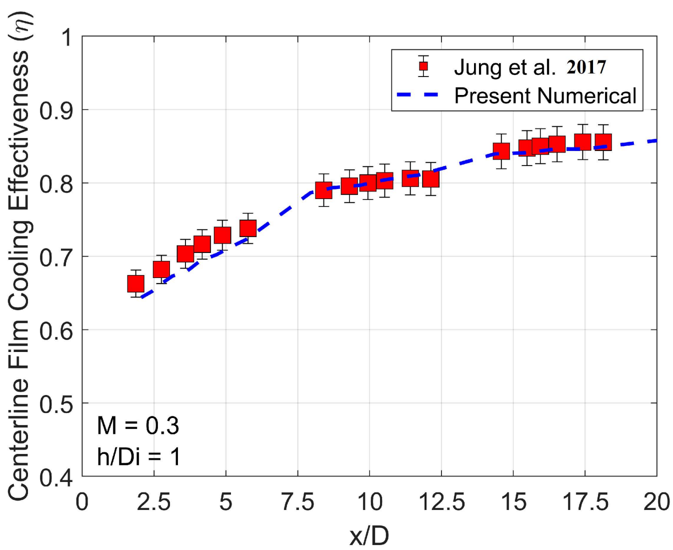


**Figure 8.** Validation of numerical model with the experimental study of Jung et al. [30] on film impingement.

These studies confirm that the present numerical methodology is capable of accurately capturing film cooling as well as the combination of film cooling and jet impingement. Hence, in the upcoming section, our validated methodology is deployed to predict the cooling performance of combined jet impingement and film cooling for aeroengine afterburner operating conditions.

### *5.2. Effect of Film and Impingement Cooling and Blowing Ratio on Temperature Distribution*

In order to understand the effects of combined film and impingement cooling on the thermal protection of an afterburner liner, the non-dimensional temperature profile is plotted along the centerline of the cooling hole, as depicted in Figure 9. The present numerical study considers three blowing ratios (M = 0.3, 0.45, 0.6). Most of the film cooling studies use a higher blowing ratio to ensure the thermal protection of components. At a higher blowing ratio, coolant lift-off is promoted due to kidney vortices and further causes poor coolant coverage [2]. Previous works on combined film and impingement cooling demonstrate [27] that films that are assisted with jet impingement cooling have a significant improvement in cooling performance (i.e., effectiveness); therefore, the thermal protection of the component can be ensured even at a low blowing ratio (i.e., less than one). For safe operation, the component's temperature must be significantly lower than the melting temperature. To clearly understand the thermal protection of such components, the surface temperature is expressed in terms of the non-dimensional temperature ($\theta_{cl}$) plotted along the centerline. A higher $\theta_{cl}$ indicates a higher surface temperature.

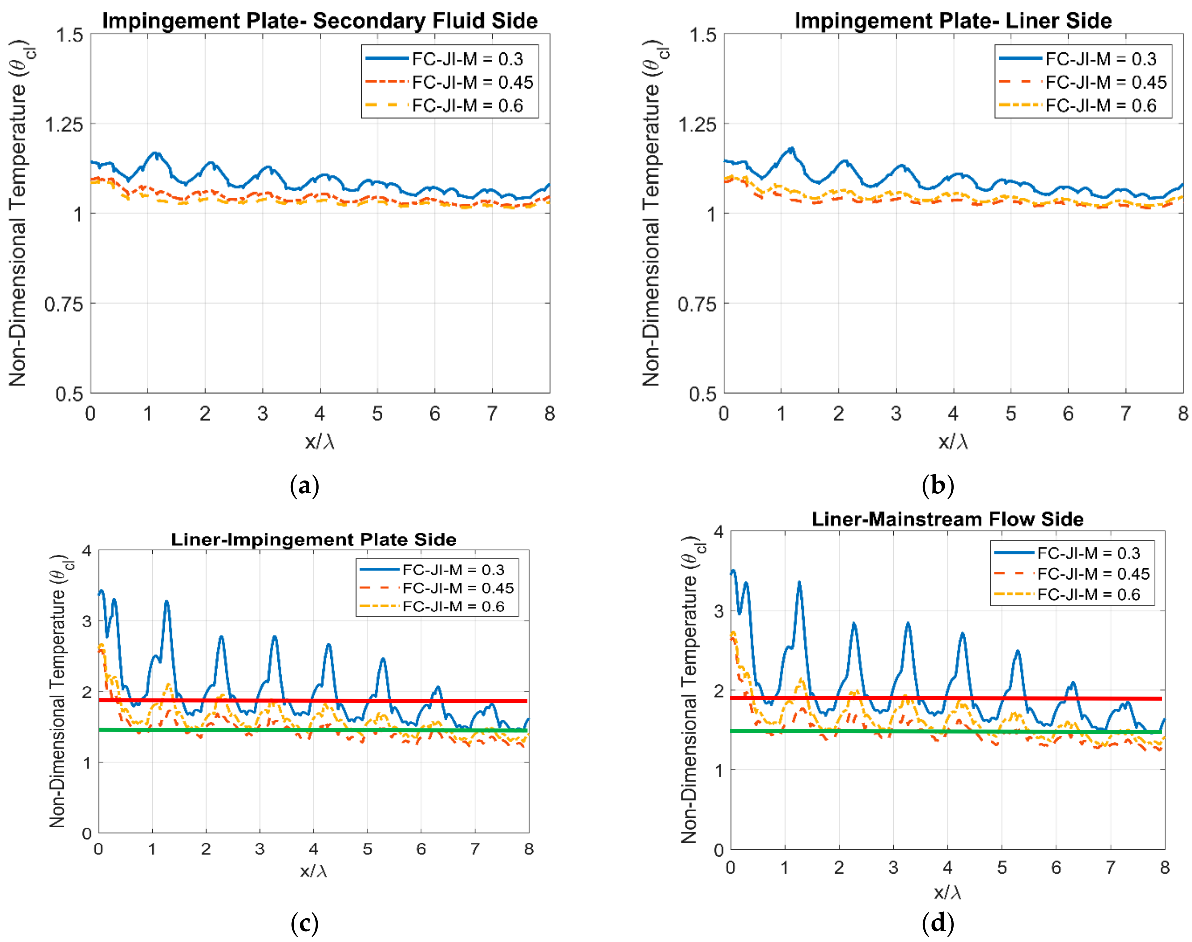


**Figure 9.** Non-dimensional wall temperature distribution: (**a**) Impingement plate—secondary fluid side; (**b**) impingement plate—liner side; (**c**) liner impingement—plate side; (**d**) liner impingement—fluid side.

Figure 9a,b represent the non-dimensional temperature ($\theta_{cl}$) variation for the impingement plate for the secondary fluid and liner side, respectively. Figure 9a,b clearly show that the non-dimensional temperature variations exhibit a wavy profile along the streamwise direction, and $x/\lambda$ = 0 to 8 with a constant decrease in the amplitude of the wave till $x/\lambda$ = 7. Moreover, with the further change in the blowing ratio from M = 0.3 to 0.6, the amplitude of the non-dimensional temperature distribution also decreases.

The phenomenon can be understood with the help of a Nusselt number distribution in Figure 10. Figure 10 clearly shows that the Nusselt number increases with the increase in the blowing ratio from M = 0.3 to 0.6. With the increase in the blowing ratio, the mass flow rate increases, which results in a larger amount of coolant passing through the impingement plate. The coolant impingement over a highly thermally conductive plate increases the heat transfer rate and therefore increases the Nusselt number, as shown in Figure 10. Moreover, at a low blowing ratio (i.e., 0.3), a higher Nusselt number can be observed to be localized near the impingement point only; however, at a higher blowing ratio (i.e., M = 0.6), a relatively uniform streamwise distribution throughout the liner surface can be observed.

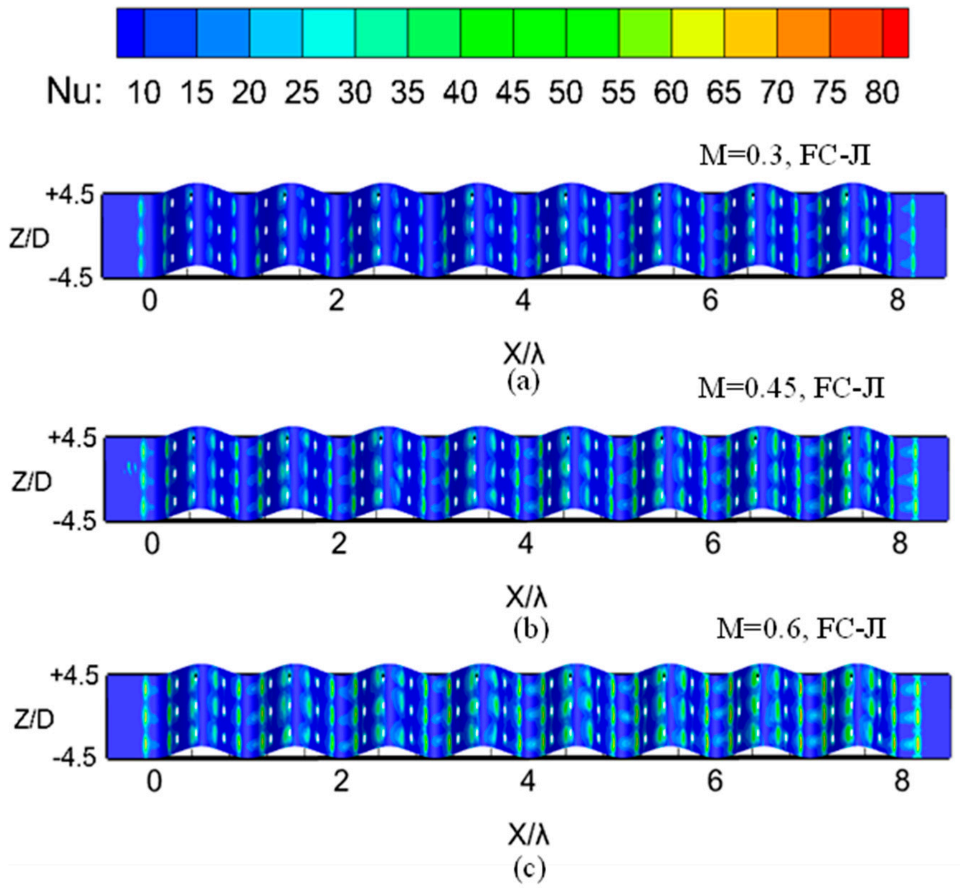


**Figure 10.** Nusselt number distribution on impingement plate (**a**) M = 0.3 FC-JI; (**b**) M = 0.45 FC-JI; (**c**) M = 0.6 FC-JI.

Figure 9c,d represent the non-dimensional temperature variation for the corrugated liner for the impingement plate and mainstream side, respectively. Figure 9c,d clearly show that, similar to those of the impingement plate, the non-dimensional temperature variations exhibit a wavy profile along the streamwise direction, and $x/\lambda$ = 0 to 8 with a monotonic decrease in amplitude. The value of $\theta$ lies in the range of 1.35 to 3.5. The recent study of Singh et al. [17,31] on corrugated afterburners suggests that a corrugated liner made up of super alloy IN738LC should be kept at a temperature of 950 K to 1050 K. These safe temperature limits correspond to values of $1.66 < \theta < 1.92$ (as shown in Figure 9c,d with horizontal lines) for the operating conditions considered in the present study. Here,

$\theta < 1.66$ indicates overcooling and $\theta > 1.91$ indicates undercooling. These values are marked by the green and red horizontal lines in Figure 9c,d. It can be observed from these figures that the cooling performance of the highest blowing ratio investigated in the present study, i.e., M = 0.6, is well within the acceptable limit from the first corrugation, i.e., $x/\lambda = 0.5$, onwards. It should also be noted that a blowing ratio of M = 0.45 also provides cooling within the safe limit except at $x/\lambda = 1.5$. However, the cooling performance at the lowest blowing ratio, i.e., M = 0.3, is not within the safe operating limit. Film cooling studies suggesting the optimum cooling configuration, such as that by Singh et al. [17,31], have been carried out at higher blowing ratios (M = 0.8 to 3). A higher blowing ratio means that a higher mass flow rate of the bleed air is required to achieve targeted cooling. This bleed air is extracted from the compressor, and it contributes towards the aerodynamic losses; hence, lower blowing ratios are desired. From the present study, it is evident that combined jet impingement and film cooling has the potential to reduce the bleed air mass flow rate requirements as a lower blowing ratio (M = 0.6), as compared to higher blowing ratios (M = 0.8 to 3) recommended by Singh et al. [17,31] for only film cooled liner.It should also be noted that the thermal barrier coating would further decrease the cooling air requirements of the combined impingement and film cooling arrangements. However, considering the thermal barrier coating is beyond the scope of the present work.

### 5.3. Effect of Film and Impingement Cooling and Blowing Ratio on Film Cooling Effectiveness

The lateral average effectiveness is an effective measure for the assessment of cooling performance. This section presents a comparison of the lateral average effectiveness and non-dimensional temperature ($\theta_{lat}$) with a range of blowing ratios from 0.3 to 0.6. Figure 11a shows the lateral average effectiveness of the corrugated liner under the combined jet impingement and film cooling. Lateral averaging is performed in the spanwise direction on the liner from $z/D = -4.5$ to $+4.5$. Figure 11a depicts that the effectiveness plot shows a wavy profile, and the peak of effectiveness indicates the row of the cooling hole. As the coolant is injected through the holes over the heated liner, the peak of effectiveness is obtained immediately downstream of the cooling holes. In contrast to the film cooling, the lateral average effectiveness increases downstream from $x/\lambda = 0$ to 8. A higher cooling effectiveness is obtained at M = 0.6 as compared to that of the other investigated blowing ratios. As discussed earlier, a higher blowing ratio means a larger flow rate of coolant, and hence a higher effectiveness is observed.

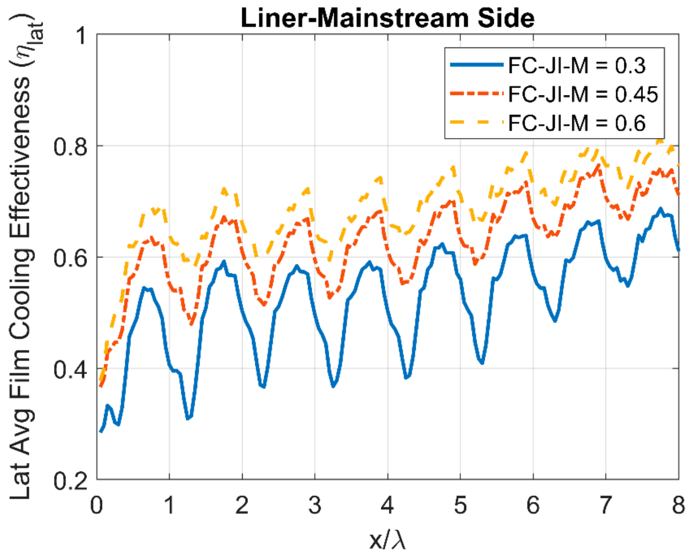


(**a**)

**Figure 11.** *Cont.*

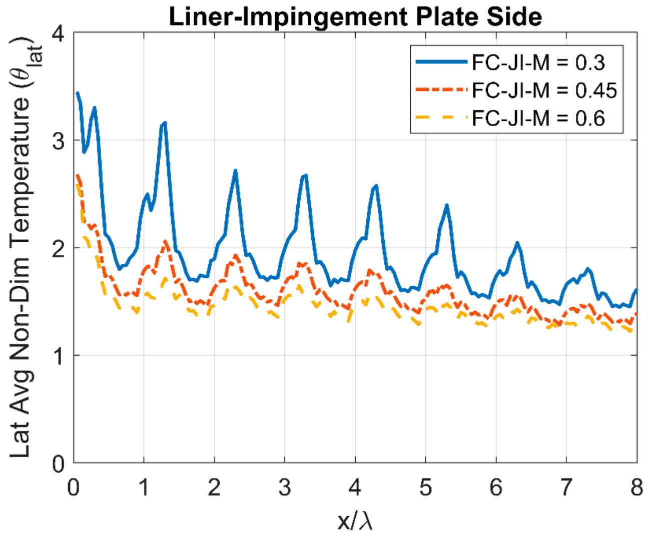


(**b**)

**Figure 11.** Distribution of (**a**) Lateral average film cooling effectiveness; (**b**) Lateral average non-dimensional temperature.

The previous section exhaustively discussed the non-dimensional temperature profile along the centerline of the cooling hole for the corrugated liner. Figure 11b depicts the trends of the lateral average non-dimensional temperature distribution over the corrugated liner. Lateral averaging is performed in the same way as discussed for the film cooling effectiveness. The lateral averaged non-dimensional temperature profile also exhibits a similar trend as shown in Figure 9d. The higher blowing ratio also results in more uniform and better lateral distribution as shown in the contour plots of the film cooling effectiveness in Figure 12.

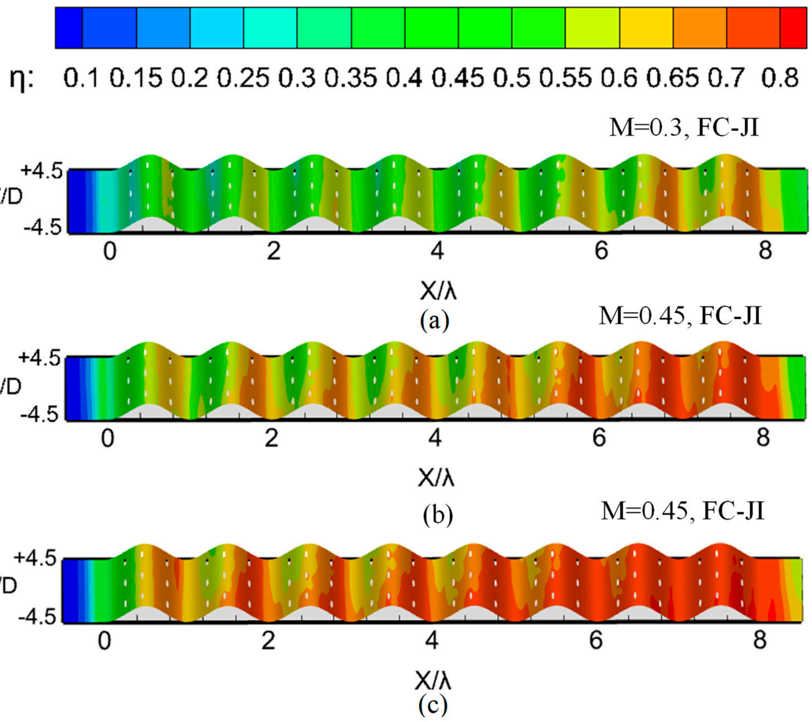


**Figure 12.** Cooling effectiveness contours for the liner—mainstream side (**a**) M = 0.3 FC-JI; (**b**) M = 0.45, FC-JI; (**c**) M = 0.6 FC-JI.

*5.4. Film–Impingement Flow Analysis*

Figure 13 shows the velocity magnitude profile at the mid plane, i.e., z/D = 0 for the different blowing ratios considered in the study. Since the mainstream velocity is the same for all three cases, there is no major change observed in the fluid flow within this section. However, the secondary flow shows a lot of dependency on the blowing ratio. The difference in the mass flow rate and its effects on the jets coming out of the impingement holes are clearly visible. At M = 0.3, the jets coming out of the impinging plate are of low intensity due to the lower pressure of the secondary flow. These jets can also be observed to be changing direction as we move away from the impingement plate, due to the local flow effect of the fluid between the liner and the impinging plate.

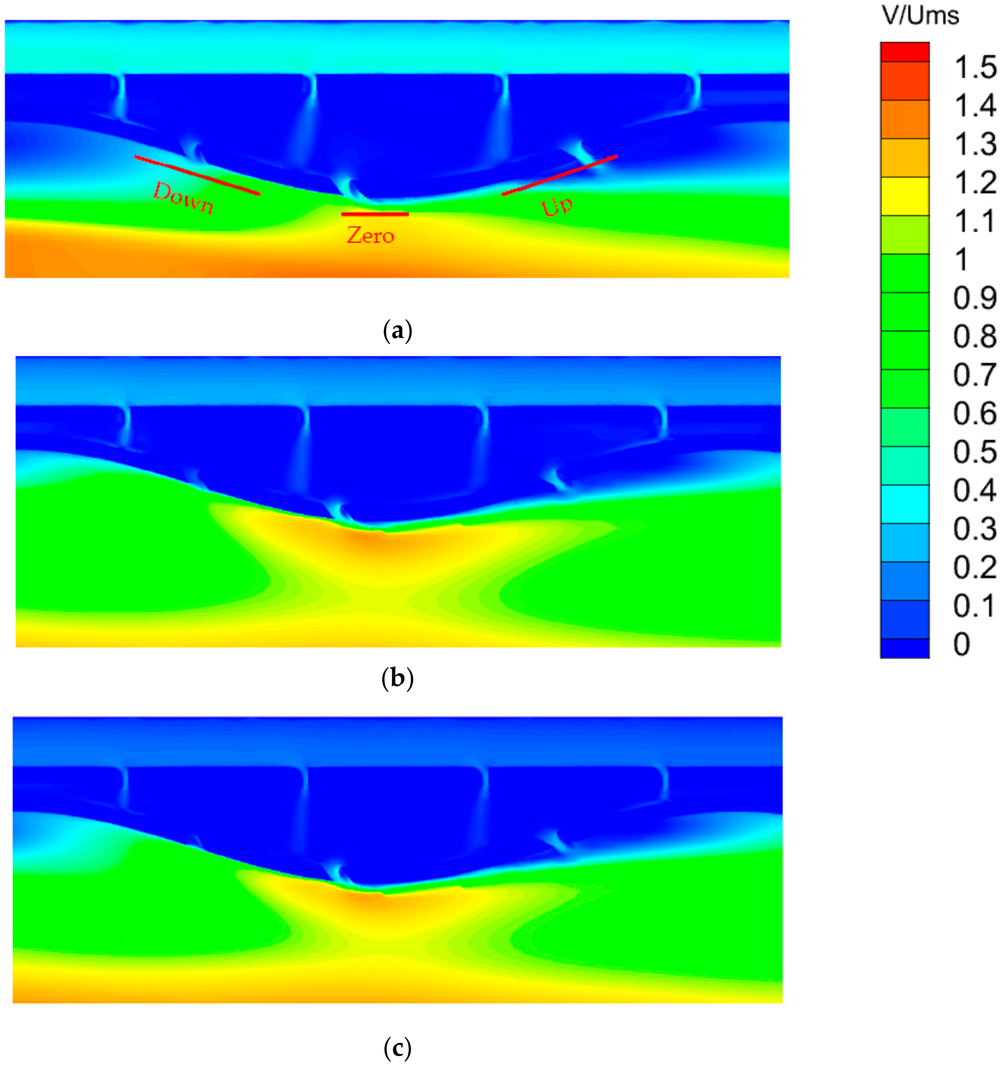


**Figure 13.** Velocity contours at z/D = 4.5 plane for (**a**) M = 0.6, (**b**) M = 0.45, and (**c**) M = 0.3.

The corrugated liner can be divided into three regions with a positive (up) slope, zero slope, and negative (down) slope, as shown in Figure 13a. The fluid ejected from the film cooling holes in the negative-sloped liner has a very low velocity magnitude. This results in a very small amount of the secondary fluid coming out of the film cooling holes facing the mainstream flow. So, a lesser amount of film cooling effectiveness is observed in this region (Figure 12). Contrary to this, the discharge of secondary fluid from the zero- and positive-sloped cooling holes is much higher and results in the formation of the low-velocity and -temperature film over the liner.

The film cooling holes over the liner are effective, but at the blowing ratio considered, they are not as effective as is required. In the applications involving lower blowing ratios, jet impingement along with film cooling is a better choice. As can be seen in Figure 14, for the points at which the jets impact the surface, a sharp change in the temperature distribution is observed over the liner surface. Similar observations have also been made with the profile of the Nusselt number (Figure 10), in which three lateral spots of higher values can be seen at each pitch of the impinging jet. Since the geometry is designed in such a way that the flow between the impingement plate and the liner is in the reverse direction to the mainstream flow, the streamlines of the jet are observed to be moving towards the mainstream inlet.

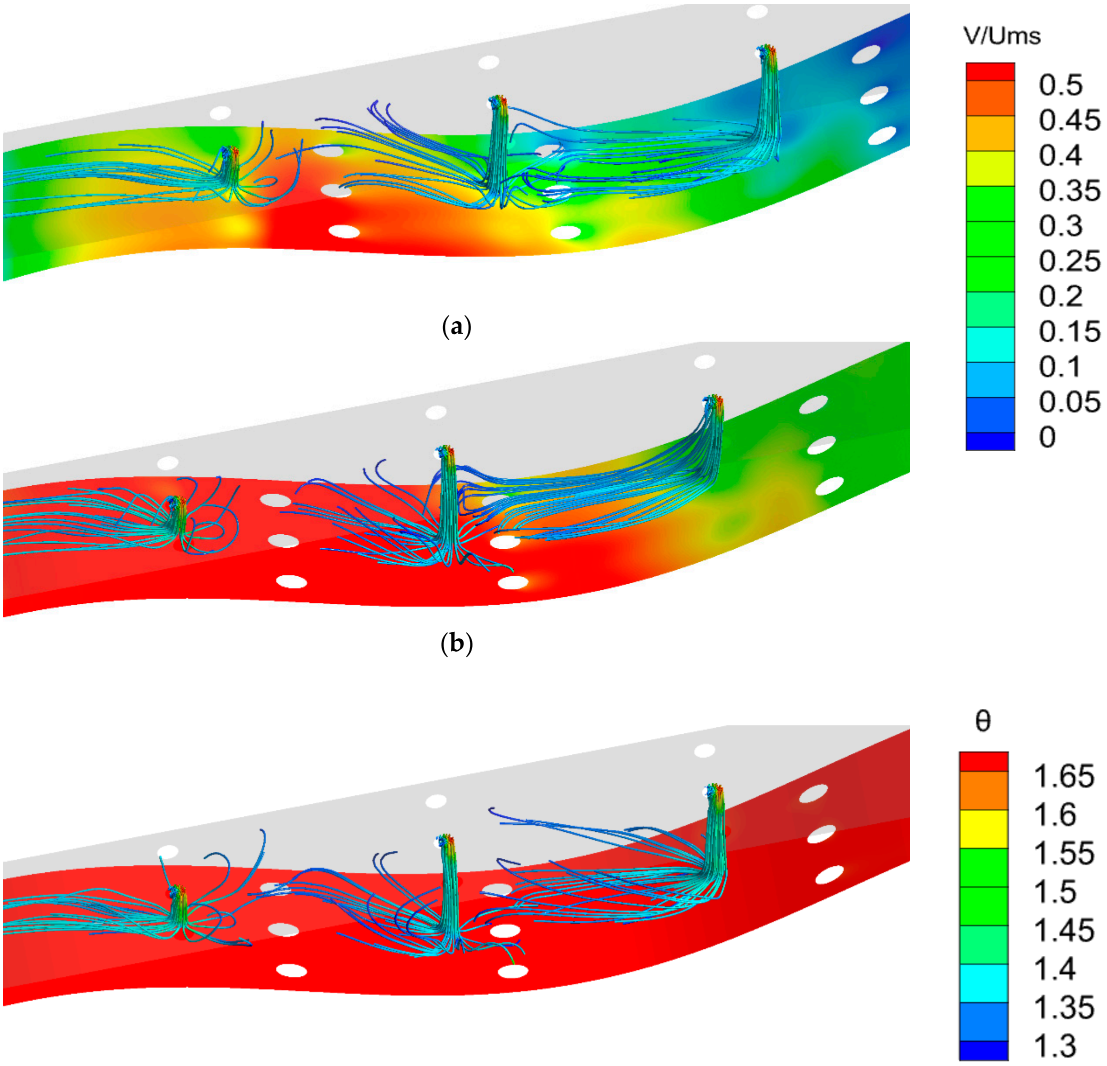


(c)

**Figure 14.** Streamlines colored according to velocity magnitude and temperature contours over the liner between $x/\lambda$ = 4.5 to 5.5 for (**a**) M = 0.6, (**b**) M = 0.45, and (**c**) M = 0.3.

## 6. Conclusions

In the present study, corrugated afterburner liner cooling effectiveness is assessed and compared with that of the combined impingement–film cooling. A numerical model is developed to predict the cooling characteristics of a corrugated liner. A detailed analysis is conducted for the temperature distribution and cooling of the corrugated liner and impingement plate for various blowing ratios (i.e., M = 0.3, 0.45, 0.6) at a constant density ratio (i.e., DR = 3.5) and h/D = 1. Based on the present study, the following inferences are drawn:

1. The non-dimensional temperature profile exhibits a wavy profile; however, the amplitude of fluctuation decreases in the downstream direction. Apart from this, the blowing ratio significantly influences the non-dimensional temperature profile for both the impingement plate and liner. The numerical results clearly indicate that with an increase in the blowing ratio, the non-dimensional temperatures are significantly reduced.
2. The complete liner section remains undercooled with a blowing ratio of 0.3. Only the entry section of the liner remains in the same condition for blowing ratios of 0.45 and 0.6. For the latter case, as the flow moves downstream, the cooling of the liner surface is perfectly balanced. The improved blowing ratio results in an increased velocity magnitude of the jets. The impinging jet reaches a velocity of 40 m/s at a blowing ratio of 0.6 and correspondingly, a Nusselt number of 80 is obtained.
3. The downward-slope section of the liner has a low film cooling effectiveness due to the weak distribution of the secondary flow in that region. The cooling hole in the zero-sloped section does not suffer from the same problem and has much better film coverage downstream of the cooling holes. The cooling holes in the positive-slope side also have a better mass flow rate of the secondary fluid, so overall this section has the best performance in each wave of the corrugated liner.
4. The current investigation shows that a lower blowing ratio (M < 0.3) is sufficient to achieve the desired surface temperature when a combined jet impingement and film cooling approach is applied. However, when film cooling is used, a greater blowing ratio (M = 1–3) is used to cool the corrugated liner in the literature.

**Author Contributions:** Conceptualization, K.S.; Methodology, S.K. and K.S.; Software, A.K.S.; Validation, A.K.S.; Formal analysis, S.K.; Writing—original draft, A.K.S.; Writing—review & editing, S.K. and K.S.; Visualization, S.K.; Supervision, K.S. All authors have read and agreed to the published version of the manuscript.

**Funding:** This research received no external funding.

**Data Availability Statement:** The data that support the findings of this study are available from the corresponding author upon reasonable request.

**Acknowledgments:** The authors are thankful to the Department of Mechanical Engineering, NIT Manipur for the Wind Tunnel test facility (Under TEQIP-III).

**Conflicts of Interest:** No potential conflict of interest was reported by the authors.

## Nomenclature

| | |
|---|---|
| $c_p$ | Specific heat (J/kgK) |
| $D_f$ | Diameter of the film cooling hole (mm) |
| $D_i$ | Diameter of the impingement hole (mm) |
| DR | Density ratio |
| e | Error, $e_a^{21} = \left\| \frac{vr_1 - vr_2}{vr_1} \right\|$ |
| g | Grid |
| GCI | Grid convergence index, $\frac{1.25 e_a^{21}}{r_{21}^p - 1}$ |
| h | Distance between jet and plate (mm) |
| htc | Heat transfer coefficient, $q''/(T_s - T_{c,in})$ (W/m$^2$K) |
| kth | Thermal conductivity (W/mK) |
| M | Blowing ratio, $\frac{\rho_c}{\rho_{ms}} \frac{U_c}{U_{ms}}$ |
| Nu | Nusselt number, $htc \times D_i / kth_{fluid}$ |
| p | Apparent order of accuracy, $\frac{1}{\ln r_{21}} \left( \left\| \ln \left\| \frac{\varepsilon_{32}}{\varepsilon_{21}} \right\| + q(p) \right\| \right)$ |
| $q''$ | Wall heat flux (W/m$^2$) |
| q(p) | $\ln \left( \frac{r_{21}^p - sa}{r_{32}^p - sa} \right)$ |

| | |
|---|---|
| $r_{21}$ | $g_2/g_1$ |
| Re | Reynolds number based on mainstream flow and cooling hole diameter |
| $t_l$ | Thickness of the liner (mm) |
| $t_{impg}$ | Impingement plate thickness (mm) |
| T | Absolute temperature (K) |
| U | Horizontal velocity component (m/s) |
| V | Velocity magnitude (m/s) |
| vr | Critical flow and heat transfer variable (e.g., $T$, $U$) |
| x | Streamwise direction (m) |
| z | Spanwise direction (m) |
| **Greek** | |
| $\alpha$ | Injection angle (degree) |
| $\varepsilon_{21}$ | $vr_2 - vr_1$ |
| $\eta$ | Film cooling effectiveness, $\frac{T_{ms}-T_{sec}}{T_{ms}-T_w}$ |
| $\theta$ | Non-dimensional temperature, $\frac{T_{ms}-T_w}{T_{ms}-T_{sec}}$ |
| $\rho$ | Density (kg/m$^3$) |
| $\mu$ | Dynamic viscosity (kg/ms) |
| $\lambda$ | Wavelength (m) |
| **Subscript** | |
| 1, 2, 3 | Different grids, viz., grid1, grid2, and grid3 |
| *cl* | Centerline |
| *fc* | Film cooling |
| *ji* | Jet impingement |
| *lat* | Lateral averaged |
| *w* | Wall |
| *sec* | Secondary |

## References


1. Tosaka, Afterburner Cut View Model, Wikipedia. 2009. (n.d.). Available online: https://en.m.wikipedia.org/wiki/File:Afterburner_cut_view_model.PNG (accessed on 23 May 2023).
2. Singh, K.; Premachandran, B.; Ravi, M.R. Experimental and numerical studies on film cooling with reverse/backward coolant injection. *Int. J. Therm. Sci.* **2017**, *111*, 390–408. [CrossRef]
3. Singh, A.K.; Singh, K.; Singh, D.; Sahoo, N. Large Eddy Simulations for Film Cooling Assessment of Cylindrical and Laidback Fan-Shaped Holes with Reverse Injection. *J. Therm. Sci. Eng. Appl.* **2021**, *13*, 031027. [CrossRef]
4. Cho, H.H.; Goldstein, R.J. Heat (Mass) transfer and film cooling effectiveness with injection through discrete holes: Part II-on the exposed surface. *J. Turbomach.* **1995**, *117*, 451–460. [CrossRef]
5. Goldstein, R.J.; Eckert, E.R.G.; Ramsey, J.W. Film cooling with injection through holes: Adiabatic wall temperatures downstream of a circular hole. *J. Eng. Gas Turbines Power* **1968**, *90*, 384–393. [CrossRef]
6. Lampard, D.; Foster, N.W. The Flow and Film Cooling Effectiveness Following Injection through a Row of Holes. *J. Eng. Power* **1980**, *102*, 584–588. [CrossRef]
7. Sinha, A.K.; Bogard, D.G.; Crawford, M.E. Film-cooling effectiveness downstream of a single row of holes with variable density ratio. *J. Turbomach.* **1991**, *113*, 442–449. [CrossRef]
8. Sen, B.; Schmidt, D.L.; Bogard, D.G. Film cooling with compound angle holes: Heat transfer. *J. Turbomach.* **1996**, *118*, 800–806. [CrossRef]
9. Pietrzyk, J.R.; Bogard, D.G.; Crawford, M.E. Effects of density ratio on the hydrodynamics of film cooling. In Proceedings of the ASME 1989 International Gas Turbine and Aeroengine Congress and Exposition, Toronto, ON, Canada, 4–8 June 1989; Volume 4. [CrossRef]
10. Moore, J.D.; Yoon, C.; Bogard, D.G. Surface Curvature Effects on Film Cooling Performance for Shaped Holes on a Model Turbine Blade. *J. Turbomach.* **2020**, *142*, 111008. [CrossRef]
11. Berhe, M.K.; Patankar, S.V. Curvature Effects on Discrete-Hole Film Cooling. *J. Turbomach.* **2017**, *121*, 781–791. [CrossRef]
12. Schwarz, S.G.; Goldstein, R.J.; Eckert, E.R.G. The influence of curvature on film cooling performance. *J. Turbomach.* **1991**, *113*, 472–478. [CrossRef]
13. Winka, J.R.; Anderson, J.B.; Boyd, E.J.; Bogard, D.G.; Crawford, M.E. Convex Curvature Effects on Film Cooling Adiabatic Effectiveness. *J. Turbomach.* **2014**, *136*, 061015. [CrossRef]
14. Funazaki, K.; Igarashi, T.; Koide, Y.; Shinbo, K. Studies on cooling air ejected over a corrugated wall: Its aerodynamic behavior and film effectiveness. In Proceedings of the ASME Turbo Expo 2001: Power for Land, Sea, and Air, New Orleans, LA, USA, 4–7 June 2001; Volume 3, pp. 1–12. [CrossRef]

15. Huang, K.; Zhang, J.; Tan, X.; Shan, Y. Experimental study on film cooling performance of imperfect holes. *Chin. J. Aeronaut.* **2018**, *31*, 1215–1221. [CrossRef]
16. Qu, L.; Zhang, J.; Tan, X.; Wang, M. Numerical investigation on adiabatic film cooling effectiveness and heat transfer coefficient for effusion cooling over a transverse corrugated surface. *Chin. J. Aeronaut.* **2017**, *30*, 677–684. [CrossRef]
17. Singh, K.; Premachandran, B.; Ravi, M.R. Experimental and numerical studies on film cooling of a corrugated surface. *Appl. Therm. Eng.* **2016**, *108*, 312–329. [CrossRef]
18. Singh, A.K.; Singh, K.; Singh, D.; Sahoo, N. Experimental and numerical analysis of film cooling performance of a corrugated surface. *Exp. Heat Transf.* **2022**, 1–23. [CrossRef]
19. Singh, A.K.; Singh, K.; Singh, D.; Sahoo, N. Experimental and Numerical Study of the Effect of Double Row Slot Injection Locations on Film Cooling Performance of a Corrugated Surface. *Exp. Heat Transf.* **2023**, 1–27. [CrossRef]
20. Panda, R.K.; Prasad, B.V.S.S.S. Conjugate heat transfer from an impingement and film-cooled flat plate. *J. Thermophys. Heat Transf.* **2014**, *28*, 647–666. [CrossRef]
21. Lee, D.H.; Kim, K.M.; Shin, S.; Cho, H.H. Thermal analysis in a film cooling hole with thermal barrier coating. *J. Thermophys. Heat Transf.* **2009**, *23*, 843–846. [CrossRef]
22. Miao, J.M.; Wu, C.Y. Numerical approach to hole shape effect on film cooling effectiveness over flat plate including internal impingement cooling chamber. *Int. J. Heat Mass Transf.* **2006**, *49*, 919–938. [CrossRef]
23. Jung, E.Y.; Lee, D.H.; Oh, S.H.; Kim, K.M.; Cho, H.H. Total cooling effectiveness on a staggered full-coverage film cooling plate with impinging jet. In Proceedings of the ASME Turbo Expo 2010: Power for Land, Sea, and Air, Glasgow, UK, 14–18 June 2010; Volume 4, pp. 1889–1896. [CrossRef]
24. Oh, S.H.; Lee, D.H.; Kim, K.M.; Cho, H.; Kim, M.Y. Enhanced Cooling Effectiveness in Full-Coverage Film Cooling System with Impingement Jets. In Proceedings of the ASME Turbo Expo 2008: Power for Land, Sea, and Air, Berlin, Germany, 9–13 June 2008. [CrossRef]
25. Singh, K.; Premachandran, B.; Ravi, M.R. Experimental assessment of film cooling performance of short cylindrical holes on a flat surface. *Heat Mass Transf.* **2016**, *52*, 2849–2862. [CrossRef]
26. Moffat, R.J. Using uncertainty analysis in the planning of an experiment. *J. Fluids Eng. Trans. ASME* **1985**, *107*, 173–178. [CrossRef]
27. Singh, K.; Udayraj. Combined film and impingement cooling of flat plate with reverse cooling hole. *Appl. Therm. Eng.* **2022**, *208*, 118224. [CrossRef]
28. Patankar, S.V. *Numerical Heat Transfer and Fluid Flow*, 1st ed.; CRC Press: Boca Raton, FL, USA, 1980. [CrossRef]
29. Celik, I.B.; Li, J. Assessment of numerical uncertainty for the calculations of turbulent flow over a backward-facing step. *Int. J. Numer. Methods Fluids* **2005**, *49*, 1015–1031. [CrossRef]
30. Jung, E.Y.; Oh, S.H.; Lee, D.H.; Kim, K.M.; Cho, H.H. Effect of impingement jet on the full-coverage film cooling system with double layered wall. *Exp. Heat Transf.* **2017**, *30*, 544–562. [CrossRef]
31. Singh, K.; Premachandran, B.; Ravi, M.R. Effect of Thermal Barrier Coating and Gas Radiation on Film Cooling of a Corrugated Surface. *ASME J. Heat Transf.* **2018**, *140*, 094504. [CrossRef]